Journal of Materials Chemistry A

PAPER

View Article Online
View Journal | View Issue

Cite this: J. Mater. Chem. A, 2017, 5, 19343

Soft-template assisted synthesis of Fe/N-doped hollow carbon nanospheres as advanced electrocatalysts for the oxygen reduction reaction in microbial fuel cells†

Lihua Zhou,[b] Chunli Yang,[b] Jing Wen,[a] Peng Fu,[b] Yaping Zhang,[a] Jian Sun,[a] Huaqian Wang[b] and Yong Yuan *[a]

Received 26th June 2017
Accepted 18th August 2017

DOI: 10.1039/c7ta05522f

rsc.li/materials-a

Heteroatom-doped hollow carbon nanospheres (HCNs) have drawn significant attention as alternative catalysts towards the oxygen reduction reaction (ORR). However, the simple and environmentally friendly synthesis of heteroatom-doped HCNs is a great challenge. Herein, an Fe/N-doped porous HCN (Fe/N-HCN) has been fabricated *via* a simple pyrolysis method using one-step synthesized poly(aniline-*co*-pyrrole) copolymer hollow nanospheres as precursors. The prepared Fe/N-HCN exhibited excellent ORR activity (onset potential of 0.02 V and half-wave potential of −0.12 V *vs.* Ag/AgCl), comparable to that of the Pt/C catalyst (onset potential of 0.01 V and half-wave potential of −0.14 V *vs.* Ag/AgCl) and superior to those of most of the reported noble metal-free carbon catalysts with hollow structures. The catalytic proficiency of the as-prepared catalyst was attributed to the abundant N and Fe atoms within the carbon lattice and a high surface area due to its hollow morphology. The as-prepared Fe/N-HCN also exhibited remarkable ORR activity in neutral solution, displaying potential application as a cathode catalyst in a microbial fuel cell (MFC). A maximum power density of 1300 ± 64 mW m^{-2} was achieved from an MFC equipped with the resultant Fe/N-HCN cathode, which outperformed that of the MFC with a Pt/C cathode. In this study, we reported a new approach for the production of Fe/N-doped carbon materials with a hollow morphology that exhibited high performance towards ORR.

1. Introduction

Sluggish oxygen reduction reaction (ORR) at the cathodes of fuel cells and metal-air batteries is considered to be one of the critical challenges for the commercialization of these energy production techniques.[1–4] Platinum (Pt)-based materials are known as the most effective catalysts to facilitate the inherent sluggish kinetic process of ORR in these techniques.[5,6] However, the utilization of Pt-based catalysts was largely hindered due to their high cost, low abundance in nature, and poor stability.[7,8] As a result, an intense search has been performed for noble metal-free catalysts with low cost, high catalytic activity, and high stability.[7–9] Cost-effective, efficient, and highly durable catalysts, such as carbon-based materials,[8,10] transition metal macrocycles,[11–14] and non-noble metal oxides,[15–18] have been investigated as potential ORR catalysts to replace Pt catalysts. However, development of more active and durable catalysts than the state-of-the-art Pt-based catalysts is still challenging.

Among various non-noble metal-based catalysts, non-noble metal/nitrogen–carbon (M/N–C) containing materials have been demonstrated as potential candidates to replace Pt catalysts for ORR due to their high activity and remarkable stability.[19,20] Experimental studies and theoretical calculations have indicated that N functionalities and/or M–N_x moieties are the main active sites for the ORR.[21] Recent studies revealed that promising M/N–C catalysts for ORR could be obtained *via* pyrolysis of carbon-supported nitrogen-rich metal complexes or simultaneous pyrolysis of a mixture of transition metal salts and nitrogen- and carbon-containing precursors. For instance, Wu *et al.* prepared a new class of M/N–C catalysts with polyaniline (PANI) and transition metals (Fe or Co) as the precursors *via* high temperature pyrolysis.[22] The resulting M/N–C showed superior activity towards ORR with low onset and half-wave potentials and excellent durability. However, the direct pyrolysis method typically results in severe aggregation, low surface area, and poor porous structure, which has negative impacts on the ORR performance. Therefore, efforts to design a new route to prepare M/N–C catalysts with high specific surface areas, rich porous structures, and homogeneous distribution of active sites

[a]School of Environmental Science and Engineering, Institute of Environmental Health and Pollution Control, Guangdong University of Technology, Guangzhou 510006, PR China. E-mail: yuanyong@soil.gd.cn; Tel: +86 20 87025872

[b]School of Chemical Engineering and Light Industry, Institute of Natural Medicine & Green Chemistry, Guangdong University of Technology, Guangzhou 510006, China

† Electronic supplementary information (ESI) available. See DOI: 10.1039/c7ta05522f

are highly desired. Hollow carbon nanospheres (HCNs) have attracted significant interest due to their unique properties such as doubled surface area, low density, and large internal void, allowing their many potential applications.[23–26] Recent studies have shown the application of the HCNs as supporting materials in the fabrication of high-performance M/N–C catalysts for ORR.[27,28] For example, Wang *et al.* demonstrated a new design for the synthesis of Fe/N-doped HCNs catalysts with high ORR performance by utilizing core–shell Cds@mSiO_2 as templates.[29] Ferrero *et al.* reported highly efficient Fe/N-doped HCN catalysts towards ORR using a nanocasting approach.[30] Notably, hard templates were frequently used to prepare these high-performance Fe/N-doped HCN catalysts. However, the removal of the template is required for hard templating, which is considered to be time consuming and severe and harmful to the environment due to the use of a strong acid.[28,31]

In this study, we demonstrated an approach for the synthesis of the Fe/N–C catalyst with a porous hollow structure without hard templating. This material was synthesized by employing aniline and pyrrole as the carbon and nitrogen precursors, $FeCl_3$ salt as the metal precursor, and Triton X-100 as the soft template, in which Triton X-100 assisted the formation of the Fe/polyaniline (PANI)/polypyrrole (Ppy) composite with a hollow structure after oxidative polymerization. The resulting hollow composite was further carbonized to convert it into Fe/N-doped HCNs. The as-prepared Fe/N-doped HCNs have high specific surface areas and small size of about 100 nm and exhibit high ORR catalytic performance and stability. Finally, we also demonstrated the remarkable utilization of the Fe/N-doped HCNs as the cathode catalyst in a microbial fuel cell (MFC).

2. Experimental methods

2.1. Synthesis of polyaniline-*co*-polypyrrole (PACP) hollow nanospheres

The schematic procedure for the synthesis of the PACP hollow nanospheres was referred from previous studies.[32,33] In brief, equal amounts of aniline and pyrrole were initially dispersed in a 20 mL Trion X-100 aqueous solution (1.6 mM) under magnetic stirring to form a solution A (Table S1†). The mixture was treated with ultrasound for 10 min to obtain a uniform solution that was maintained at 4 °C for 20 min. Then, 20 mL of solution B with 0.2 M ammonium peroxydisulfate (APS) aqueous solution cooled at 4 °C was added to the solution A. The resulting solution was stirred for 5 min and then maintained at 4 °C for oxidative polymerization. Finally, the polymer product was obtained through filtration of the mixture reactants until the filtrate became colorless after 24 h of oxidative polymerization reaction and dried at 60 °C for 12 h. The same procedure was used to synthesize Fe-doped PACP hollow nanospheres; however, solution B was obtained by the dissolution of APS and $FeCl_3 \cdot 6H_2O$ with a ratio of 2 : 1.[34] For comparison, solid Fe-doped PACP nanospheres were also synthesized by changing the quantitative relation of aniline and pyrrole (Table S1†). After being washed and dried at 60 °C for 12 h, the solid products were carbonized at 900°Cat a heating rate of 5 °C min^{-1} under a N_2 atmosphere for 2 h. The black carbonized product was obtained after being washed with a 1 M HCl solution under stirring overnight and then washed with deionized water, which was termed as an Fe/N-doped HCN (Fe/N-HCN). For comparison, the as-prepared PACP was directly carbonized at 900 °C at a rate of 5 °C min^{-1} under a N_2 atmosphere for 2 h, and the resulting carbon material was termed as N-HCN. In addition, the PACP solid nanospheres were converted into Fe-doped solid carbon nanospheres (Fe/N-SCN) *via* pyrolysis.

2.2. Structural characterization

The morphology and composition of the samples were analyzed using a transmission electron microscope (TEM, JEM-2100F, JEOL, Ltd., Tokyo, Japan), a field emission scanning electron microscope (FE-SEM, S-4800, Hitachi, Ltd., Tokyo, Japan), and an EDAX energy dispersive spectrometer (EDS). The crystal structures of these materials were measured by an X-ray diffractometer (XRD, X' Pert Pro, Philips). Raman spectra were obtained using a LabRAM Aramis confocal microscope Raman spectrometer system (Renishaw Instruments, England). The surface compositions of the materials were examined by X-ray photoelectron spectroscopy (XPS, Thermal Scientific ESCALAB 250Xi spectrometer, USA). Nitrogen sorption analysis was conducted at 300 °C using a sorptometer (Model 1800, Carlo Erba Instruments, Italy). The Brunauer–Emmett–Teller (BET) equation was used to calculate the nitrogen adsorption data. The pore size distribution (PSD) plot was obtained from the adsorption branch of the isotherm based on the Barrett–Joyner–Halenda (BJH) model.

2.3. Electrocatalytic activity measurements

Electrocatalytic properties of the as-prepared catalysts were investigated *via* a conventional three-electrode cell using an electrochemical workstation (CHI660D, Shanghai Chenhua Instruments Co., China) controlled at room temperature. A Ag/AgCl electrode and a platinum plate were employed as the reference and counter electrodes, respectively. A glassy carbon ring disk electrode (RDE, 5 mm in diameter) served as the working electrode after 10 μL catalyst ink was coated on its surface. The catalyst ink was obtained by mixing the carbon catalyst powder (2.0 mg) with 200 μL ethanol, 100 μL distilled water, and 10 μL Nafion (5%) solution in an ultrasonic bath. Cyclic voltammograms (CVs) were obtained in an oxygen-saturated and nitrogen-saturated KOH solution (0.1 M). Linear sweep voltammetry (LSV) polarization curves were measured at a sweep rate of 10 mV s^{-1} at the rotating speeds varying from 800 to 2400 rpm. The Koutecky–Levich (K–L) plots were obtained though the LSV curves, and the number of electrons transferred was calculated by the K–L equation:

$$j^{-1} = j_k{}^{-1} + (B\omega^{0.5})^{-1} \quad (1)$$

$$B = 0.62nF(D_{O_2})^{\frac{2}{3}}\nu^{-\frac{1}{6}}C_{O_2} \quad (2)$$

where j and j_k are the measured and kinetic limiting current densities, respectively, ω is the rotation speed, n is the number of electrons transferred in the reduction of O_2, F is the Faraday constant (F = 96 485 C mol^{-1}), D_{O_2} and C_{O_2} are the diffusion

coefficient and bulk concentration of O_2 in 0.1 M KOH, respectively, and ν is the kinematic viscosity of the electrolyte ($\nu = 0.01$ cm^2 s^{-1}).

2.4. MFC configuration and operation

A cubic air-cathode, single-chamber MFC was constructed as previously described,[35] wherein a graphite fiber brush (2.5 cm in both diameter and length) served as the anode and a Pt/C or Fe/N-HCN cathode was used as the cathode. The cathode was prepared by dispersing either the as-prepared catalysts or Pt/C on the catalytic layer of cathodic carbon cloth. The catalyst dosage of these two materials was 2.0 and 0.5 mg m^{-2}, respectively. Sodium acetate solution (1.0 g L^{-1}) in a 50 mM phosphate buffer (PBS, pH = 7.0) was used as a medium to feed the batch mode MFC. The medium was supplemented with a 12.5 mL L^{-1} mineral solution and a 5 mL L^{-1} vitamin solution. All MFCs were inoculated with the effluent of well-operated MFCs. The MFCs were operated in triplicate in a 30 °C incubator, and the mean values were presented.

3. Results and discussion

3.1. Preparation of the Fe/N-doped hollow carbon nanospheres

The facile procedure with a soft template for the preparation of the Fe/N-HCN is depicted in Fig. 1a, which involves facile fabrication of Fe-doped hollow nanosphere precursors and thermal treatment for carbonization. The Fe-doped PACP hollow nanospheres were prepared *via* the oxidation polymerization of comonomers (aniline and pyrrole) in the presence of Triton X-100 and iron salt.[32,33] As explored by Zhou *et al.*,[32] the formation of the PACP hollow structure was due to the different hydrophobic properties of aniline and pyrrole in the hydrophobic Triton X-100 micelles. At first, the comonomers were located in the inner side of micelles with a higher concentration than that in the bulk solution due to their hydrophobicity. The copolymerization of aniline and pyrrole mainly took place at the micelle–water interface as it was difficult for the hydrophilic oxidant APS to penetrate into the hydrophobic micellar palisade layer. A well-defined hollow structure could be formed because more hydrophobic pyrrole quickly diffused from the micellar interiors for copolymerization. Fig. S1† displays the typical SEM and TEM images of the resultant Fe-doped PACP hollow nanospheres. The SEM image showed that the products were composed of well-defined nanospheres, and the corresponding TEM image revealed that the PACP nanospheres had hollow interiors at their centers. The average diameter of hollow nanospheres is about 125 nm, the inner diameter is about 60 nm, and the shell thickness is about 32 nm. *Via* the same procedures, Fe-PACP solid nanospheres were also synthesized. The synthesized nanosphere precursors were then carbonized at 900 °C under a N_2 atmosphere to convert them into Fe/N-doped carbon-based catalysts. As previously reported, carbon catalysts derived from aromatic precursors, such as polyaniline and polypyrrole, exhibit a better combination of activity and durability for the ORR than the catalysts derived from nonaromatic precursors.[22,36] The SEM images in Fig. 1b, e, and h show that all products display well-defined nanospheres. In the magnified TEM image shown in Fig. 1c and f, it can be observed that the hollow structure is well retained in the N-HCN and Fe/N-HCN materials. The total and inner diameters of N-HCN and Fe/N-HCN were similar (Fig. 1d and g), which were about 100 nm and 50 nm, respectively. The carbonized hollow spheres are smaller than their precursors; this can be explained based on the shrinkage during carbonization. It is noteworthy that a tedious template removing process is not required for the synthesis of N-HCN and Fe/N-HCN because the soft template can also be directly converted into carbon materials during pyrolysis. For comparison, excepting the solid structure, Fe/N-SCN showed a similar spherical structure as N-HCN and Fe/N-HCN. As shown in Fig. 1h and i, Fe/N-SCN displayed well-defined nanospheres without a hollow structure; this indicated that the hollow structure could be changed by adjusting the mole ratio of aniline and pyrrole. Fe/N-SCN had similar particle size distribution as N-HCN and Fe/N-HCN (Fig. 1j). The TEM-EDS elemental mapping suggested uniform distribution of C, N, and Fe elements in the Fe/N-HCN (Fig. 1k).

3.2. Characterization of the Fe/N-HCN catalysts

Raman spectroscopy and X-ray diffraction (XRD) patterns were used to explore the structure of the as-prepared carbon materials. Fig. 2a depicts the Raman spectrum of N-HCN, Fe/N-HCN, and Fe/N-SCN, in which the patterns of Raman spectra can be deconvoluted into 4 bands. The first peak at *ca.* 1220 cm^{-1} is potentially associated with the presence of sp^3 rich phases (polyene-like structures).[37] The second peak at *ca.* 1350 cm^{-1} is usually assigned to the D band, which is associated with curved sheets, defects, and dangling bonds in the carbonaceous structure.[38] The third peak at *ca.* 1524 cm^{-1} can be attributed to the presence of an amorphous sp^2 phase and/or Fe–N_x bonds in carbon materials.[37,39] The intensity of the Raman bands at 1220 and 1524 cm^{-1} is significantly increased for Fe/N-HCN and Fe/N-SCN as compared to that for N-HCN; this suggests that Fe/N-HCN and Fe/N-SCN contain a higher ratio of amorphous carbon than N-HCN.[40] Additionally, the huge magnitude of lines observed at *ca.* 1524 cm^{-1} shows that both Fe/N-HCN and Fe/N-SCN samples are highly disordered along the c-axis and/or enriched in Fe–N_x active sites.[39] The final peak at 1590 cm^{-1} is assigned to the G band, which often corresponds to the graphitic carbon with an sp^2 electronic configuration.[38] The intensity ratios of the D band to G band (I_D/I_G) are 0.63, 0.92, and 0.94 for N-HCN, Fe/N-HCN, and Fe/N-SCN, respectively, suggesting high degree of disordering in the graphite structure of these carbon materials. The high I_D/I_G values of Fe/N-HCN and Fe/N-SCN might be due to the defects introduced *via* Fe doping. It is noteworthy that there is a clear shift in the position of the G peaks for Fe/N-HCN and Fe/N-SCN; this can also result from the high degree of disordering in their graphitic structures caused by Fe doping.[37]

Further structural characterization was conducted by XRD (Fig. 2b), which exhibits two major diffraction peaks at 24° and 44° for all samples. These two peaks were assigned to the {002}

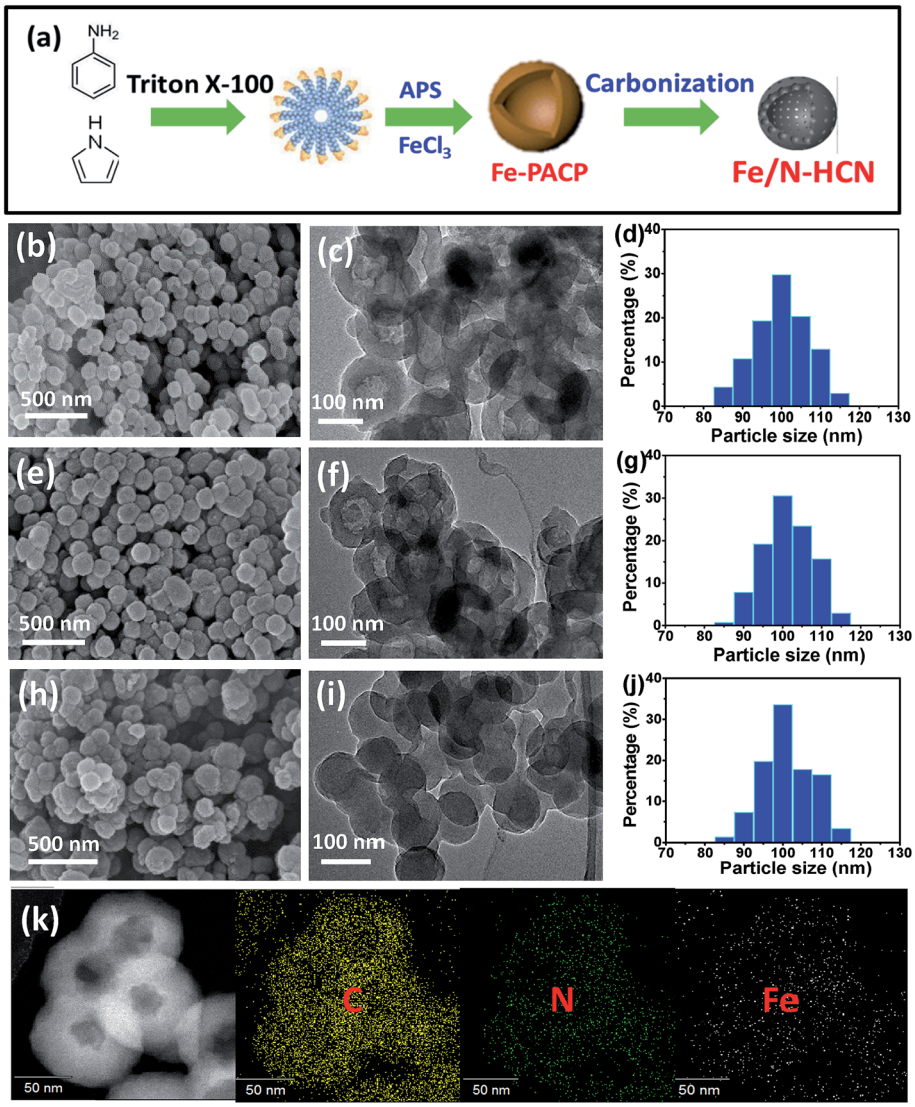

Fig. 1 (a) Schematic of the procedures used for the synthesis of Fe/N-HCN; SEM and TEM images and the corresponding particle size distribution of N-HCN (b, c, and d), Fe/N-HCN (e, f, and g), and Fe/N-SCN (h, I, and j), respectively; the TEM-EDS elemental mapping of the as-prepared Fe/N-HCN (k).

and {101} diffraction planes of the hexagonal graphite, respectively, suggesting that the carbon nanomaterials contained a steady graphitic structure.[41] Fig. 2c and d show the N_2 adsorption-desorption isotherms and pore size distributions of the resulting carbon catalysts. As shown in Fig. 2c, N-HCN, Fe/N-HCN, and Fe/N-SCN displayed a type IV isotherm with hysteresis, which was indicative of porous structures. The calculated total BET surface areas were 893.3, 853.1, and 322.8 $m^2\ g^{-1}$ for N-HCN, Fe/N-HCN, and Fe/N-SCN, respectively (Table S2†). It is noteworthy that the BET surface areas of N-HCN and Fe/N-HCN were much higher than that of Fe/N-SCN due to the hollow core of these materials. The pore size distribution of these three products is shown in Fig. 2d, which exhibits that the size range of the pores is mainly from 1.7 to 10.0 nm. The diameters of these pores were centered at 3.39, 4.73, and 4.32 nm, and the corresponding total pore volumes were 0.76, 0.75, and 0.35 $cm^3\ g^{-1}$ for N-HCN, Fe/N-HCN, and Fe/N-SCN, respectively (Table S2†). Notably, the resulting carbon materials displayed the microporous surface areas of 723.0, 675.1, and 249.8 $m^2\ g^{-1}$ and micropore volumes of 0.37, 0.34, and 0.13 $cm^3\ g^{-1}$ for N-HCN, Fe/N-HCN, and Fe/N-SCN, respectively, which contributed to the major surface area and volume of these materials.

As revealed by the XPS survey spectra, Fe/N-HCN contained four main elements, *i.e.* C, O, N, and Fe with the atomic percentages of 86.2, 7.5, 4.2, and 1.8%, respectively; this suggested the successful doping of N and Fe in these hollow carbon nanospheres. It should be pointed out that the N doping was self-derived from the aniline and pyrrole precursors. Table S2† shows that the prepared solid nanospheres have the same chemical composition as Fe/N-HCN. Fig. 3a shows the high-resolution C 1s spectra of Fe/N-HCN, which displays five major components corresponding to C–C/C=C (284.5 eV), C=N/C–O (285.0 eV), C=O/C–N (286.7 eV), O–C=O (289.2 eV), and

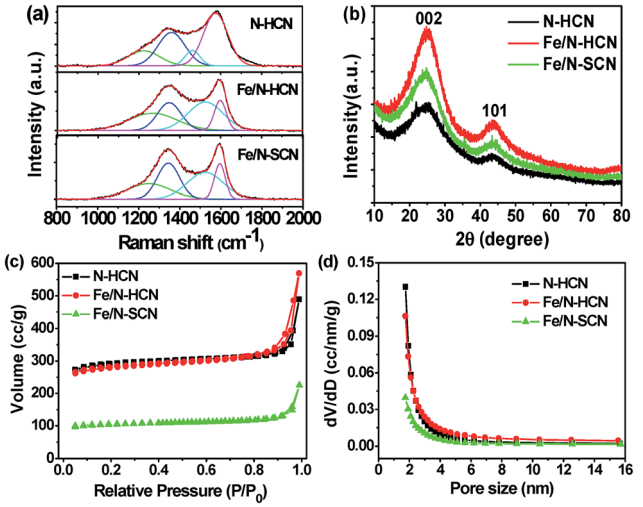

Fig. 2 (a) Raman spectrum, (b) XRD pattern, (c) N_2 adsorption and desorption isotherms, and (d) pore size distributions of N-HCN, Fe/N-HCN, and Fe/N-SCN.

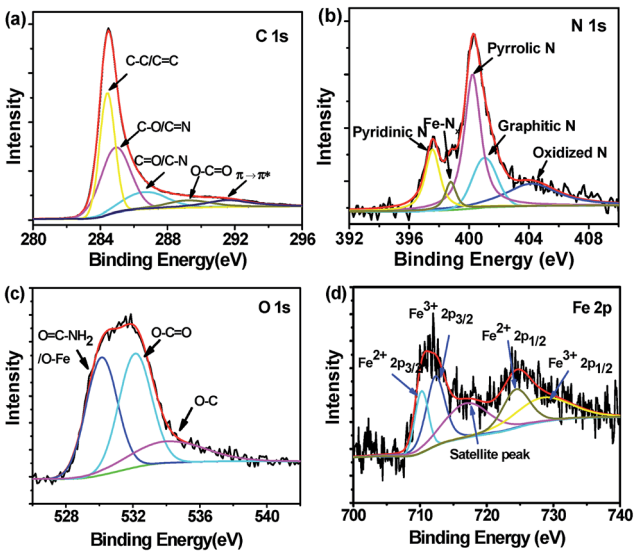

Fig. 3 High-resolution C 1s (a), N 1s (b), O 1s (c), and Fe 2p (d) XPS spectra of the Fe/N-HCN.

$\pi \rightarrow \pi^*$ transition (291.5 eV).[37,42,43] High resolution N 1s XPS spectra in Fig. 3b demonstrates the presence of five sub-peaks at 397.5, 398.7, 400.3, 401.5, and 404.1, which can be assigned to pyridinic, Fe–N_x, pyrrolic, graphitic, and oxidized N, respectively.[44] The presence of the Fe–N bonding in deconvoluted N 1s signals provided evidence for the formation of Fe–N_x groups in Fe/N-HCN. Similarly, the O 1s spectrum was found to entail three oxygen moieties (Fig. 3c). The peaks at the binding energies of 530.5, 533.0, and 534.6 eV might be assigned to O=C–NH_2, O–C, and O=C, respectively.[35] In addition, the peak at 530.5 eV might also be attributed to the O–Fe moieties, suggesting the existence of the iron oxide phase.[45,46] The high resolution Fe 2p spectra are shown in Fig. 3d, where the peaks at 710.2 and 712.3 eV can be attributed to the binding energy of $2p_{3/2}$ orbitals of Fe^{2+} and Fe^{3+} species and the peaks at 724.3 and 728.9 eV can be ascribed to the binding energy of $2p_{1/2}$ orbitals of Fe^{2+} and Fe^{3+} species, respectively. The satellite Fe $2p_{3/2}$ peak at 717.0 eV also indicated the existence of the iron oxide phase in the carbon material.[47] Additionally, the peak at 710.2 eV in the Fe $2p_{3/2}$ XPS spectrum indicates the presence of Fe–N_x bonding resulting from Fe ions coordinated to N.[48,49] For comparison, XPS measurements were conducted to examine N-HCN and Fe/N-SCN under the same conditions, showing similar status as Fe/N-HCN for these main chemical elements (Fig. S2†).

3.3. Electrocatalytic activities of Fe/N-HCN towards ORR

The electrocatalytic activity of Fe/N-HCN towards ORR was evaluated *via* CV and LSV techniques in an O_2 or N_2 saturated 0.1 M KOH solution at a scan rate of 10 mV s^{-1} at room temperature. The CV of the Fe/N-HCN electrode in the N_2-saturated 0.1 M KOH electrolyte showed the typical pseudocapacitive behavior (Fig. 4a). A cathodic current peak at −0.09 V *vs.* Ag/AgCl with an onset potential of 0.02 V *vs.* Ag/AgCl was observed when the Fe/N-HCN-coated electrode was scanned in an O_2-saturated KOH solution. This peak potential was similar to that of Pt/C at −0.10 V *vs.* Ag/AgCl with an onset potential of 0.01 V. Moreover, the ORR peak current density of Fe/N-HCN reached about 0.65 mA cm^{-2} by subtracting the background current, which was only slightly lower than that of the Pt/C catalyst (0.73 mA cm^{-2}). These results demonstrated the remarkable electrocatalytic ability of Fe/N-HCN towards ORR. RDE measurements were conducted by scanning the potential in the range from +0.2 to −0.8 V at a rotation rate of 1600 rpm to further compare the electrocatalytic performance of Fe/N-HCN with that of Pt/C and other synthesized catalysts. As shown in

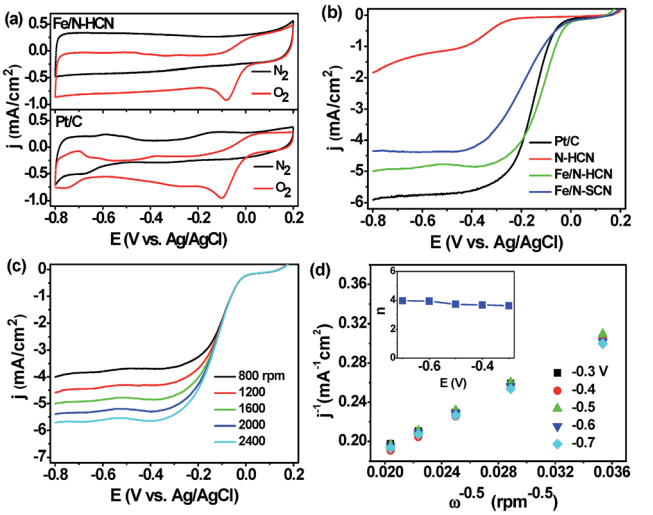

Fig. 4 (a) CV curves for Pt/C and Fe/N-HCN in N_2-saturated and O_2-saturated 0.1 M KOH solutions at a scan rate of 10 mV s^{-1}; (b) RDE curves for N-HCN, Fe/N-HCN, Fe/N-SCN, and Pt/C in O_2-saturated 0.1 M KOH solutions at a scan rate of 10 mV s^{-1} and a rotation speed of 1600 rpm; (c) RDE curves of Fe/N-HCN at different rotation rates; (d) K–L plots at different potentials for Fe/N-HCN (inset: the calculated number of electrons transferred (n)).

Fig. 4b, Fe/N-HCN has an onset potential of 0.02 V *vs.* Ag/AgCl and a half-wave potential of −0.12 V *vs.* Ag/AgCl. Remarkably, Fe/N-HCN displayed the most positive onset potential and highest current density as compared to N-HCN and Fe/N-SCN. It is important to highlight that Fe/N-HCN shows even more positive onset and half-wave potentials than commercial Pt/C (onset potential of 0.01 V *vs.* Ag/AgCl and half-wave potential of −0.14 V). The catalytic activity of Fe/N-HCN matches that of most of the hollow carbon materials in the current state of research (Table S3†). The catalytic activity of Fe/N-HCN is higher than that of Fe/N-SCN; this demonstrates that the hollow structure is beneficial for high catalytic activity. As revealed by the surface area measurements, the surface area of Fe/N-HCN was almost double that of Fe/N-SCN. The increased surface area due to the hollow structure was believed to provide more active sites towards ORR.[50,51] In addition, similar surface areas were obtained from Fe/N-HCN and N-HCN, but the catalytic activity of Fe/N-HCN was much higher than that of N-HCN. The result demonstrates that the Fe–N_x active sites may contribute to the remarkable electrocatalytic activity of Fe/N-HCN although more systematic study is still required to identify the inherent mechanism of Fe–N_x active sites for catalyzing the ORR.

To further reveal the electrocatalytic performance of Fe/N-HCN and Pt/C, RDE measurements were also carried out at different rotational speeds. Fig. 4d and S3† show the corresponding K–L plots obtained from the RDE measurements in which the inverse current density (j^{-1}) linearly depends on the inverse of the square root of the rotation speed ($\omega^{-1/2}$). According to the slope of the K–L plots, the number of electrons transferred during the ORR process was close to four for Fe/N-HCN, indicating a four-electron transfer pathway. Remarkable stability and tolerance to the crossover effect was usually achieved from carbon-based catalysts. As shown in Fig. S4a,† the stability and tolerance of Fe/N-HCN to methanol were examined. The addition of 3 M methanol did not impact the catalytic current of Fe/N-HCN towards the ORR; this suggested that the as-prepared Fe/N-HCN catalyst was tolerant to methanol. In addition, the ORR current density of the Fe/N-HCN electrode decreased by only 8.0% over 10 000 s of continuous operation at −0.3 V *vs.* Ag/AgCl, but the Pt/C catalyst displayed a 20% decrease in current density (Fig. S4b†). These results suggested that Fe/N-HCN had promising stability and remarkable tolerance to crossover effects, offering potential applications in fuel cells.

3.4. Application of Fe/N-HCN as the cathode catalyst in an MFC

Microbial fuel cells (MFCs) are an emerging technology that can convert organic substrates into electricity using microorganisms as catalysts, which have promising applications such as in wastewater treatment, electricity generation, biosensing, and pollutant bioremediation.[52,53] In MFCs, oxygen, as the most sustainable electron acceptor in the cathode, is frequently employed to receive the electrons generated from the bioanode to complete the electric circuit. However, the commercial applications of MFCs have been hindered by the high cost and low stability of the Pt-based catalysts that are used to accelerate the sluggish ORR in the cathode. Recent advancements in the cathode catalysts of the MFC suggest that non-metal carbon-based catalysts are potential alternative catalysts for the ORR.[11] Herein, we evaluated the feasibility of the as-prepared Fe/N-HCN as a catalyst towards ORR in a single-chamber air-cathode MFC. The MFCs are generally operated under near neutral pH condition, which is an optimal environment for bacterial growth.[35] Thus, the catalytic activity of the Fe/N-HCN was also evaluated in a neutral phosphate buffer solution (pH = 7.0). As shown in Fig. 5a, the Fe/N-HCN showed well-defined cathodic oxygen reduction peaks in an O_2-saturated phosphate buffer solution (PBS, pH 7.0); this indicated the electrocatalytic activity of the catalyst. As shown in Fig. 5b, the LSV measurements showed that Fe/N-HCN had the most positive onset potential and highest current density as compared to N-HCN and Fe/N-HCN in a neutral solution. It is noticed that Fe/N-HCN had very similar limiting current density as the Pt/C catalyst; this indicated the remarkable electrocatalytic activity of the Fe/N-HCN towards ORR in a neutral solution. As depicted in Fig. 5c, the current density of the Fe/N-HCN increased as the rotation speed was enhanced from 800 to 2400 rpm. The K–L plots displayed good linearity at various potentials (Fig. 5d). The *n* value for the Fe/N-HCN was calculated to be 3.7–4.0, indicating that this catalyst was effective for a 4-electron ORR in the neutral solution. A single-chamber air-cathode MFC with an Fe/N-HCN as the cathode catalyst was constructed, in which a wet-proofed carbon cloth loaded with Fe/N-HCN or Pt/C was used as an air cathode and coupled with a bioanode (Fig. 6a). As shown in Fig. 6b, a power density of 1300 ± 64 mW m^{-2} was achieved from the MFC with the Fe/N-HCN cathode, which was slightly higher than that obtained from the MFC with the Pt/C cathode (1132 ± 60 mW m^{-2}). For these MFCs, the individual cathode potentials differed, whereas the individual anode potentials were similar (Fig. 6c); this demonstrated that the differences in

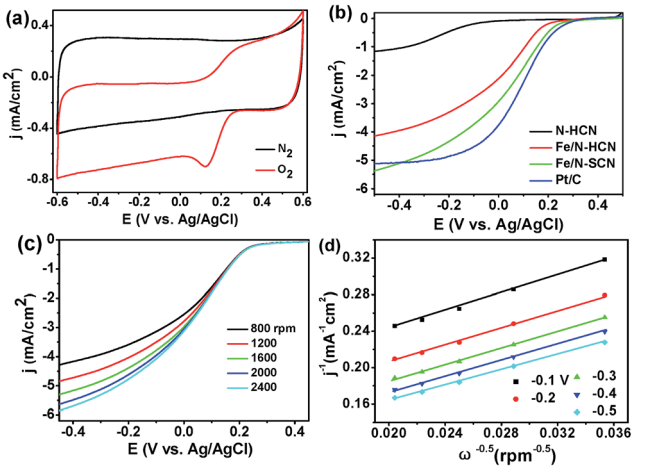

Fig. 5 (a) CV curves for the Fe/N-HCN in a N_2-saturated and O_2-saturated PBS solution (pH = 7.0) at a scan rate of 10 mV s^{-1}; (b) RDE curves for N-HCN, Fe/N-HCN, Fe/N-SCN, and Pt/C at a scan rate of 10 mV s^{-1} and a rotation speed of 1600 rpm; (c) RDE curves of Fe/N-HCN in an O_2-saturated PBS solution at different rotation rates; (d) K–L plots at different potentials for Fe/N-HCN.

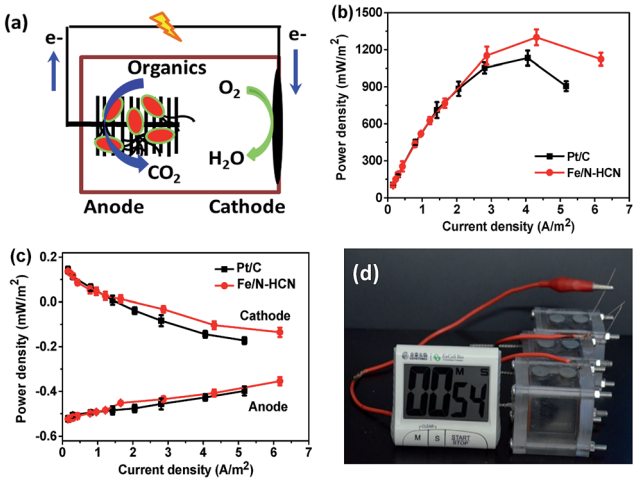

Fig. 6 (a) Schematic of the basic configuration of a single chamber air-cathode MFC, in which a wet-proofed carbon cloth loaded with Fe/N-HCN is used as an air cathode and a biofilm-attached graphite brush is used as a bioanode; (b) polarization curves of the MFCs equipped with Fe/N-HCN and Pt/C cathodes; (c) the individual potentials of the anode and cathode in the MFCs; (d) image of three-series MFCs drives a timer to work.

the performance originated from variations in catalytic activities. Finally, as a demonstration, three MFCs in series with the Fe/N-HCN cathodes could drive a timer (Fig. 6d). The results indicate that the Fe/N-HCN is a good candidate to replace the high-cost Pt as a cathode catalyst in MFCs.

4. Conclusions

In this study, we demonstrated a facile and effective method to produce Fe and N-co-doped hollow carbon nanospheres using one-step synthesized poly(aniline-*co*-pyrrole) copolymer hollow nanospheres as the precursors. The unique features of the resultant Fe/N-HCN include a high specific surface area due to the hollow morphology and a large number of N and Fe–N_x active sites within the carbon framework due to the use of polyaniline and polypyrrole and iron salt as the carbon and metal precursors, respectively. As a result, the Fe/N-HCN displayed high ORR activity and stability in alkaline media, which outperformed the commercial Pt/C catalyst. Specifically, the Fe/N-HCN exhibited good catalytic activity in a neutral solution, providing a potential alternative to the cathode of the MFCs. The present study offers a new route for the synthesis of a Fe/N-co-doped hollow carbon catalyst with high activity and low cost.

Conflicts of interest

There are no conflicts to declare.

Acknowledgements

This study was jointly supported by the National Natural Science Foundation of China (No. 51678162), Guangzhou City Science–Technology Project (Nos. 201707010250 and 2014Y2-00194), Guangdong Natural Science Funds for Distinguished Young Scholar (No. 2014A030306033), Natural Science Fund of Guangdong province (No. 2016A030310351), Science and Technology Planning Project of Guangdong Province (2014A020216042), and Guangdong Special Fund for Public Welfare Research and Capacity Building (No. 2015A030302075).

References

1 M. Lefèvre, E. Proietti, F. Jaouen and J. P. Dodelet, *Science*, 2009, **324**, 71–74.
2 W. Yang, T. Fellinger and M. Antonietti, *J. Am. Chem. Soc.*, 2010, **133**, 206–209.
3 S. Chen, Z. Wei, X. Qi, L. Dong, Y. Guo, L. Wan, Z. Shao and L. Li, *J. Am. Chem. Soc.*, 2012, **134**, 13252–13255.
4 Y. Jiang, Y. Lu, X. Wang, Y. Bao, W. Chen and L. Niu, *Nanoscale*, 2014, **6**, 15066–15072.
5 R. F. Service, *Science*, 2007, **315**, 172.
6 K. Gong, F. Du, Z. Xia, M. Durstock and L. Dai, *Science*, 2009, **323**, 760–764.
7 G. Ma, R. Jia, J. Zhao, Z. Wang, C. Song, S. Jia and Z. Zhu, *J. Phys. Chem. C*, 2011, **115**, 25148–25154.
8 S. Gao, Y. Chen, H. Fan, X. Wei, C. Hu, H. Luo and L. Qu, *J. Mater. Chem. A*, 2014, **2**, 3317–3324.
9 Z. Luo, D. Yang, G. Qi, J. Shang, H. Yang, Y. Wang, L. Yuwen, T. Yu, W. Huang and L. Wang, *J. Mater. Chem. A*, 2014, **2**, 20605–20611.
10 K. Meng, Q. Liu, Y. Huang and Y. Wang, *J. Mater. Chem. A*, 2015, **3**, 6873–6877.
11 B. Merzougui, A. Hachimi, A. Akinpelu, S. Bukola and M. Shao, *Electrochim. Acta*, 2013, **107**, 126–132.
12 L. Lin, Q. Zhu and A. Xu, *J. Am. Chem. Soc.*, 2014, **136**, 11027–11033.
13 S. Mao, Z. Wen, T. Huang, Y. Hou and J. Chen, *Energy Environ. Sci.*, 2014, **7**, 609–616.
14 H. Wang, X. Bo, A. Wang and L. Guo, *Electrochem. Commun.*, 2013, **36**, 75–79.
15 T. N. Lambert, D. J. Davis, W. Lu, S. J. Limmer, P. G. Kotula, A. Thuli, M. Hungate, G. Ruan, Z. Jin and J. M. Tour, *Chem. Commun.*, 2012, **48**, 7931–7933.
16 Z. Ma, X. Huang, S. Dou, J. Wu and S. Wang, *J. Phys. Chem. C*, 2014, **118**, 17231–17239.
17 K. B. Liew, R. W. D. Wan, M. Ghasemi, K. S. Loh, M. Ismail, S. S. Lim and J. X. Leong, *Int. J. Hydrogen Energy*, 2015, **40**, 11625–11632.
18 C. W. Woon, H. R. Ong, K. F. Chong, K. M. Chan and M. M. R. Khan, *Procedia Chem.*, 2015, **16**, 640–647.
19 E. Negro, A. H. A. M. Videla, V. Baglio, A. S. Aricò, S. Specchia and G. J. M. Koper, *Appl. Catal., B*, 2014, **166–167**, 75–83.
20 A. H. A. M. Videla, S. Ban, S. Specchia, L. Zhang and J. Zhang, *Carbon*, 2014, **76**, 386–400.
21 Z. Y. Wu, P. Chen, Q. S. Wu, L. F. Yang, Z. Pan and Q. Wang, *Nano Energy*, 2014, **8**, 118–125.
22 G. Wu, K. L. More, C. M. Johnston and P. Zelenay, *Science*, 2011, **332**, 443–447.
23 T. Yang, J. Liu, R. Zhou, Z. Chen, H. Xu, S. Qiao and M. Monteiro, *J. Mater. Chem. A*, 2014, **2**, 18139–18146.

24 S. Chen, J. Bi, Y. Zhao, L. Yang, C. Zhang, Y. Ma, Q. Wu, X. Wang and Z. Hu, *Adv. Mater.*, 2012, **24**, 5593–5597.
25 Y. Hu, J. O. Jensen, W. Zhang, L. N. Cleemann, W. Xing, N. J. Bjerrum and Q. Li, *Angew. Chem., Int. Ed.*, 2014, **53**, 3675–3679.
26 G. Ma, R. Jia, J. Zhao, Z. Wang, C. Song, S. Jia and Z. Zhu, *J. Phys. Chem. C*, 2011, **115**, 25148–25154.
27 J. Wei, Y. Liang, X. Zhang, G. P. Simon, D. Zhao, J. Zhang, S. Jiang and H. Wang, *Nanoscale*, 2015, **7**, 6247–6254.
28 J. Sanetuntikul, T. Hang and S. Shanmugam, *Chem. Commun.*, 2014, **50**, 9473–9476.
29 Y. Wang, A. Kong, X. Chen, Q. Lin and P. Feng, *ACS Catal.*, 2015, **5**, 3887–3893.
30 G. A. Ferrero, K. Preuss, A. Marinovic, A. B. Jorge, N. Mansor, J. L. B. Dan, A. B. Fuertes, M. Sevilla and M. M. Titirici, *ACS Nano*, 2016, **10**, 5922–5932.
31 J. Sanetuntikul, C. Chuaicham, Y. Choi and S. Shanmugam, *J. Mater. Chem. A*, 2015, **3**, 15473–15481.
32 C. Zhou, J. Han, G. Song and R. Guo, *J. Polym. Sci., Part A: Polym. Chem.*, 2008, **46**, 3563–3572.
33 F. Xu, Z. Tang, S. Huang, L. Chen, Y. Liang, W. Mai, H. Zhong, R. Fu and D. Wu, *Nat. Commun.*, 2015, **6**, 7221–7233.
34 Q. F. Yi, Y. H. Zhang, X. P. Liu and Y. H. Yang, *Sci. China: Chem.*, 2014, **57**, 739–747.
35 X. Ma, C. Feng, W. Zhou and H. Yu, *J. Power Sources*, 2016, **307**, 105–111.
36 X. Yuan, X. L. Ding, C. Y. Wang and Z. F. Ma, *Energy Environ. Sci.*, 2013, **6**, 1105–1124.
37 I. Abidat, C. Morais, S. Pronier, N. Guignard, J. D. Comparot, C. Canaff, T. W. Napporn, A. Habrioux, A. S. Mamede, J. F. Lamonier and K. B. Kokoh, *Carbon*, 2017, **111**, 849–858.
38 X. Fan, Z. Yang and N. He, *RSC Adv.*, 2015, **5**, 15096–15102.
39 I. Martinaiou, A. Sharaei, F. Grimm, H. Zhang, C. Wittich, S. Klemenz, S. J. Dolique, H. J. Kleebe, R. W. Stark and U. I. Kramm, *Electrochim. Acta*, 2017, **243**, 183–196.
40 Z. Liu, K. Xiao, H. Guo, X. Ning, A. Hu, Q. Tang, B. Fan, Y. Zhu and X. Chen, *Carbon*, 2017, **117**, 163–173.
41 M. Zhou, C. Yang and K. Y. Chan, *Adv. Energy Mater.*, 2014, **4**, 1400840–1400845.
42 X. Liu, W. Zhou, L. Yang, L. Li, Z. Zhang, Y. Ke and S. Chen, *J. Mater. Chem. A*, 2015, **3**, 8840–8846.
43 Y. Xie, C. Tang, Z. Hao, Y. Lv, R. Yang, X. Wei, W. Deng, A. Wang, B. Yi and Y. Song, *Faraday Discuss.*, 2014, **176**, 393–408.
44 Y. Qian, P. Du, P. Wu, C. Cai and D. F. Gervasio, *J. Phys. Chem. C*, 2016, **120**, 9884–9896.
45 S. Lee, J. Y. Cheon, W. J. Lee, S. O. Kim, S. H. Joo and S. Park, *Carbon*, 2014, **80**, 127–134.
46 Z. Zhang, Y. Qin, M. Dou, J. Ki and F. Wang, *Nano Energy*, 2016, **30**, 426–433.
47 T. Palaniselvam, V. Kashyap, S. N. Bhange, J. B. Baek and S. Kurungot, *Adv. Funct. Mater.*, 2016, **26**, 2150–2162.
48 Z. Y. Wu, X. X. Xu, B. C. Hu, H. W. Liang, Y. Lin, L. F. Chen and S. H. Yu, *Angew. Chem., Int. Ed.*, 2015, **127**, 8297–8301.
49 L. Lin, Q. Zhu and A. W. Xu, *J. Am. Chem. Soc.*, 2014, **136**, 11027–11033.
50 H. Zhang, Y. Wang, D. Wang, Y. Li, X. Liu, P. Liu, H. Yang, T. An, Z. Tang and H. Zhao, *Small*, 2014, **10**, 3371–3378.
51 Y. Li, H. Zhang, Y. Wang, P. Liu, H. Yang, X. Yao, D. Wang, Z. Tang and H. Zhao, *Energy Environ. Sci.*, 2014, **7**, 3720–3726.
52 K. Rabaey and W. Verstraete, *Trends Biotechnol.*, 2005, **23**, 291–298.
53 M. D. Lorenzo, T. P. Curtis, I. M. Head and K. Scott, *Water Res.*, 2009, **43**, 3145–3154.

